Cell Reports
Physical Science

CellPress
OPEN ACCESS

Article

DNA controls the dimerization of the human FoxP1 forkhead domain

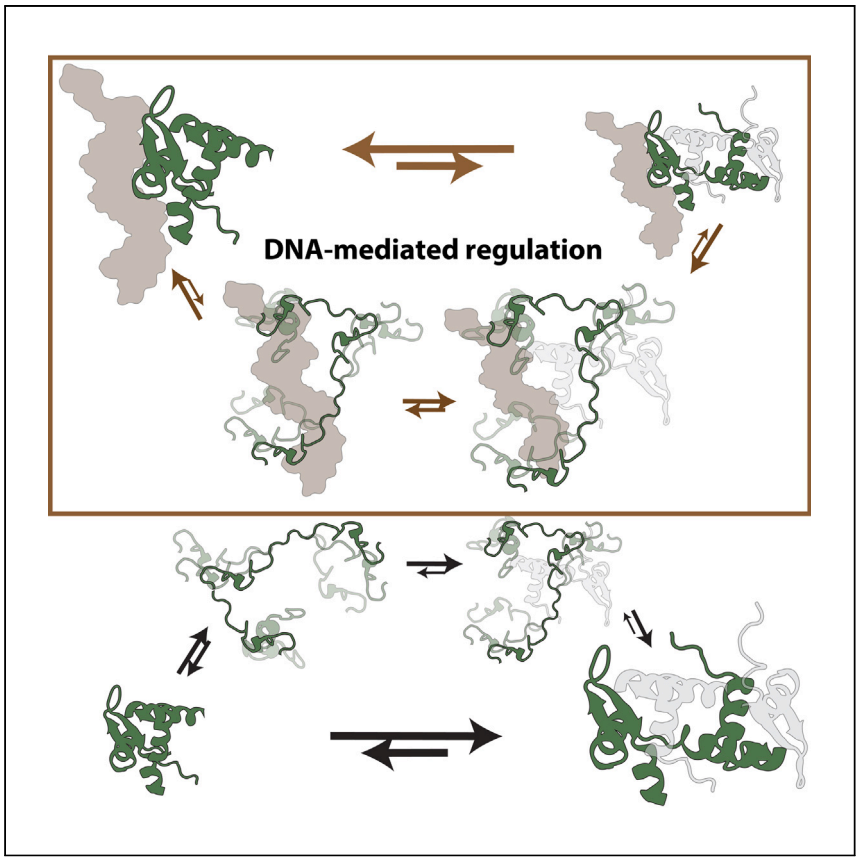

The structural characteristics of human FoxP proteins play a vital role in both their dimerization and functionality. Kolimi et al. show that DNA binding induces a higher structural disorder within the DNA-binding domain of the FoxP protein, having implications for the dimerization, its ability to interact with the DNA, and overall function.

Narendar Kolimi, Jake Ballard, Thomas Peulen, ..., Jorge Babul, Exequiel Medina, Hugo Sanabria

exequiel.medinago@uchile.cl (E.M.)
hsanabr@clemson.edu (H.S.)

Highlights

The FKH domain of FoxP1 is structurally dynamic in monomer and dimeric conditions

The dimerization of the FKH domain stabilizes the intramolecular dynamics

The presence of DNA destabilizes the dimeric FKH domain and promotes a disordered state

The presence of DNA favors the monomeric state of the FKH domain

Kolimi et al., Cell Reports Physical Science 5, 101854
March 20, 2024 © 2024 The Authors.
https://doi.org/10.1016/j.xcrp.2024.101854

Cell Reports
Physical Science

CellPress
OPEN ACCESS

Article

DNA controls the dimerization of the human FoxP1 forkhead domain

Narendar Kolimi,[1] Jake Ballard,[1] Thomas Peulen,[2] Rajen Goutam,[1] Francis X. Duffy III,[1] César A. Ramírez-Sarmiento,[3,4] Jorge Babul,[5] Exequiel Medina,[1,5,*] and Hugo Sanabria[1,6,*]

SUMMARY

Transcription factors (TFs) regulate gene expression by binding to specific DNA sequences and gating access to genes. Even when the binding of TFs and their cofactors to DNA is reversible, indicating a reversible control of gene expression, there is little knowledge about the molecular effect DNA has on TFs. Using single-molecule multiparameter fluorescence spectroscopy, molecular dynamics simulations, and biochemical assays, we find that the monomeric form of the forkhead (FKH) domain of the human FoxP1 behaves as a disordered protein and increases its folded population when it dimerizes. Notably, DNA binding promotes a disordered FKH dimer bound to DNA, negatively controlling the stability of the dimeric FoxP1:DNA complex. The DNA-mediated reversible regulation on FKH dimers suggests that FoxP1-dependent gene suppression is unstable, and it must require the presence of other dimerization domains or cofactors to revert the negative impact exerted by the DNA.

INTRODUCTION

Transcription factors (TFs) are vital proteins that regulate transcription by controlling access to DNA depending on changes in the 3D structure of the genome.[1–3] Generally, TFs bind specific DNA sequences promoting the structural stability of the TF:DNA complex.[4]

Cofactors and other TF machinery regulate TF function via homotypic and heterotypic interactions including the basic-helix-loop-helix motifs,[5] leucine zippers,[6] and Zn^{2+} fingers domains.[7–9] Moreover, TF binding to DNA sometimes promotes sequential homotypic or heterotypic TF interactions,[10,11] as in the case of pioneer TFs,[12] and often this leads to dimerization of TFs in complex with DNA.[13] As a result, gene regulation is frequently portrayed as a unidirectional action of TFs on DNA following the reaction: TF + DNA → TF:DNA → TF:TF:DNA → function,[14] where the function results in gene activation or suppression (Figure 1A).

Evidently, the reversibility of the reaction limits the duration and action of transcriptional complexes. Although multiple models have demonstrated the involvement of regulators in the on/off switch of the complex formation,[15] the exploration into the stability of the transcriptional complex bound to DNA remains limited. This includes investigating the reverse order of the reaction (function → TF:TF:DNA → TF:DNA → TF + DNA) and understanding the active role of DNA as an integral component of gene regulation, aspects that have not been extensively explored.

To study the role of DNA in the reversible reaction, we use the P subfamily of Fox TFs[16] (FoxP) as a model system. FoxP TFs contain a leucine zipper domain (LZ) that

[1]Department of Physics and Astronomy, Clemson University, Clemson, SC 29634, USA

[2]Rudolf-Virchow-Zentrum – Center for Integrative and Translational Bioimaging, Haus D15, Josef-Schneider-Straße 2, 97080 Würzburg, Germany

[3]Institute for Biological and Medical Engineering, Schools of Engineering, Medicine and Biological Sciences, Pontificia Universidad Católica de Chile, Santiago 7820436, Chile

[4]ANID – Millennium Science Initiative Program – Millennium Institute for Integrative Biology (iBio), Santiago 8331150, Chile

[5]Departamento de Biología, Facultad de Ciencias, Universidad de Chile, Las Palmeras 3425, Casilla 653, Santiago 7800003, Chile

[6]Lead contact

*Correspondence: exequiel.medinago@uchile.cl (E.M.), hsanabr@clemson.edu (H.S.)

https://doi.org/10.1016/j.xcrp.2024.101854

This is an open access article under the CC BY-NC-ND license (http://creativecommons.org/licenses/by-nc-nd/4.0/).

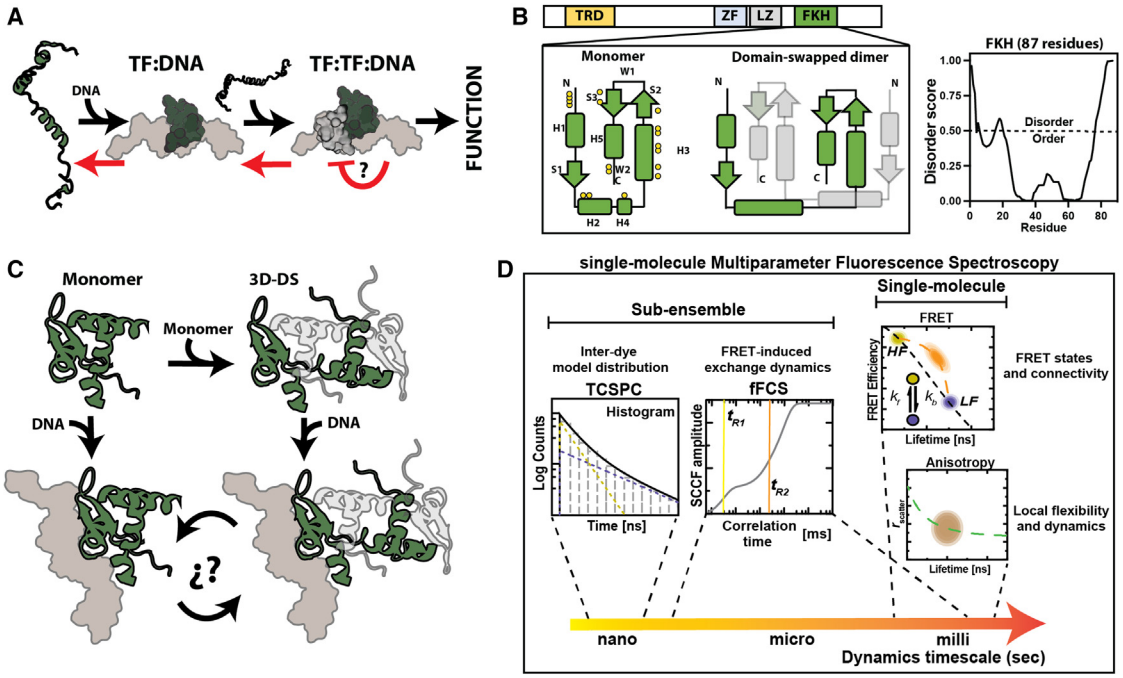

Figure 1. Insights on the molecular mechanism of the transcription factor (TF):DNA regulation of the FKH domain in FoxP1

(A) Schematics of the known mechanism by which TFs perform their function (unidirectional in black arrows), showing in red arrows the unknown molecular processes that must occur to turn off the function and dissemble the transcription complex, highlighting the unsolved question about how the structural changes adopted by the transcriptional complex can regulate its function. Generally, the binding of the monomer to the DNA promotes the binding of another monomer to the same site. However, FoxP proteins associate with different symmetry, where each monomer can bind a different DNA molecule (not shown in this model for simplicity).

(B) Domain organization of human FoxP proteins. All human FoxP proteins contain a forkhead (FKH), a leucine zipper (LZ), a Zinc Finger, and a *trans*-repressor (TRD) domain. The secondary structure of the forkhead domain (FKH) in the monomeric and its 3D-DS dimer form are shown as blocks and arrows where H stands for α-Helix and S for β-Strand. The yellow circles represent the DNA-binding regions of the protein. The disorder prediction server PONDR[68] is also shown for the FKH domain.

(C) Three-dimensional structure of the monomer and 3D-DS dimer of FoxP1, indicating the different TF:DNA complexes (monomer:DNA and 3D-DS:DNA, DNA in brown). We study these conditions with single-molecule multiparameter fluorescence spectroscopy (smMFS) and present the open question that leads to the reversible process.

(D) smMFS allows us to determine the structural dynamics of the FKH domain in its monomeric and dimeric forms and when interacting with DNA. Time-resolved fluorescence (time-correlated single-photon counting, TCSPC) provides information about the heterogeneity of FRET-derived distance distribution within populations in single-molecule FRET (smFRET) multidimensional histograms. Fluctuation analysis (filtered FCS) helps derive the temporal indication of the changes in FRET. Single-molecule fluorescence anisotropy (smFA) allows the determination of local flexibility changes.

is involved in association with bZIP proteins and shares a highly conserved forkhead-box DNA-binding domain (FKH) (Figure 1B) required for DNA binding. The FKH domain dimerizes in the absence and presence of DNA three-dimensional domain swapping (3D-DS) via an in route disordered like intermediate state,[17] behaving differently from the canonical TFs where the monomers do not independently bind to DNA motifs or like the widely DNA-mediated dimerization via folding-upon-binding by which TFs adopt a ternary active complex with the cognate DNA.

As the 3D-DS dimer contains an intertwined structure (Figure 1B), each monomer is allowed to contact distant regions of the DNA, forming quaternary (2TFs:2DNA) assemblies[18] (Figure 1C). Previously, we described that the FKH domain of FoxP1 assemblies in 3D-DS dimers is facilitated by intrinsically disordered regions (Figure 1B), highlighting the importance of structural disorder as a dimerization promoter.[17] Moreover, knowing that the FKH domain is highly conserved among FoxP proteins, we showed that DNA promotes heterodimerization by increasing the conformational flexibility within the FKH domain.[19]

CellPress
OPEN ACCESS

Considering that the FKH domain can bind DNA as a monomer and as a dimer,[20–23] we explore two functional unsolved questions regarding the presence of the DNA: (1) What structural rearrangements occur in the monomer and the dimer in the presence of the DNA? (2) How does the DNA impact the dimerization equilibrium? (Figure 1C). These questions are not trivial, as different dimerization-affecting mutations on the FKH domain[20,24–28] have been related to immune and intellectual dysfunction, suggesting that the active form of the protein is the dimer.

Using the FKH domain of the human FoxP1 TF and a combination of experimental and computational methods, we characterized how the monomeric and the dimeric forms of the FKH domain behave in the absence and presence of DNA. By employing single-molecule multiparameter fluorescence spectroscopy (smMFS) (Figure 1D) and molecular dynamics simulations, we monitored the local and global structural changes of the FKH. Further, we used ensemble biochemical assays to evaluate the effect of DNA in the dimerization. We identified that DNA binding promotes a disordered fuzzy-like FKH dimer, likely directly impacting the dimer-dependent gene suppression function of FoxP proteins. The negative feedback mechanism over the FKH dimerization introduces DNA as a crucial cofactor for gene regulation. Instead of the conventional "folding-upon-binding" model, where the active TF:DNA complex is structurally stabilized, DNA binding destabilizes the protein. Our findings point to a DNA-mediated allostery that provides a DNA-mediated reversible (TF:DNA⇌TF:TF:DNA⇌function) gene regulatory function.

RESULTS

The monomeric state of FoxP1's FKH domain exchanges between folded and disordered states

To investigate the structure and dynamics of the unknown FoxP1 monomer solution, we employed Förster resonance energy transfer (FRET).[29] FRET allowed us to precisely measure distances and dynamics between donor and acceptor fluorophores.[30,31] Specifically, we utilized two FRET-labeled double-cysteine variants: S57C/V78C (referred to as C57-C78) and L18C/V78C (referred to as C18-C78)[17] (Figure 2A). The C18-C78 variant provided insights into the backbone opening required in adopting the 3D-DS dimer. On the other hand, the C57-C78 variant enabled us to observe structural changes in the DNA-interacting helix H3. Both FRET variants were labeled with Alexa 488 (donor, D) and Alexa 647 (acceptor, A), and their measurements were conducted in the monomeric state using the procedures outlined in the materials and methods section.

For each variant, we first analyzed the donor's lifetimes in the presence of the acceptor, as the changes in the lifetime is an indicator of FRET.[32,33] We found that all variants were successfully fitted to two FRET states (Table S1). With this information, we compared the intensity-based FRET efficiency, E, and the donor's average lifetime in the presence of the acceptor ($\langle\tau_{D(A)}\rangle_f$) for each single molecule, generating a two-dimensional single-molecule (sm-2D) counting histograms (Figure 2B and Table S2). The sm-2D over these observables (1) allows us to determine D-A distances, (2) allows us to detect the presence of observable dynamics during the observation of the molecules, and (3) can discriminate models, e.g., by comparing FRET lines to experiments. This way, sm-2D histograms can reveal the kinetic connectivity of states with different FRET levels.[34,35] We have successfully applied this approach to multiple systems.[17,36,37]

Both FRET variants showed a predominant population around FRET efficiencies of 0.1–0.2, which we defined as low FRET (LF). Although, the C57-C78 showed an

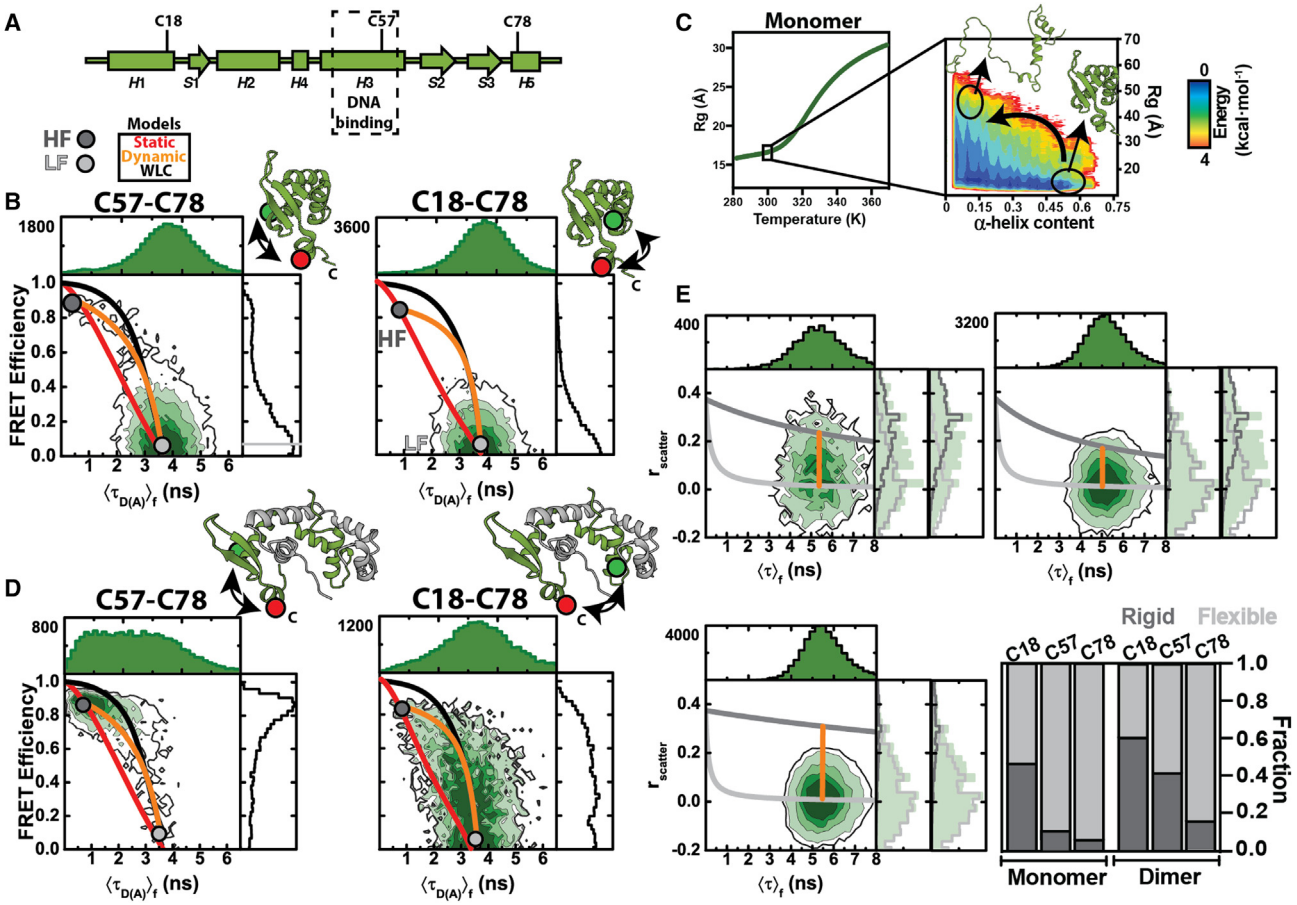

Figure 2. Structural dynamics of the monomeric and dimer FoxP1 FKH

(A) Topology of the FKH domain showing different secondary structure elements (rectangles represent α-helices and arrows β-sheets), the position of the different labeling reactions (C18, C57 years C78), and the region that specifically binds the DNA.

(B) Single-molecule multiparameter fluorescence spectroscopy sm-2D histograms of the FRET efficiency and the average fluorescence lifetime of the donor in the presence of acceptor $\langle\tau_{D(A)}\rangle_f$ for the monomer variants C57-C78 and C18-C78. Each FRET state was determined in terms of the donor's lifetimes in the presence of the acceptor and shown as a filled circle (HF in dark gray circle, LF in light gray circle). The representative structure for the HF state with the monitored region by the FRET pair (donor, green; acceptor, red) is shown. The three physical FRET models (static, WLC, and dynamic) are represented as lines in the sm-2D. Correction parameters are found in Table S2.

(C) Changes in the radius of gyration (*R*g) as a function of the temperature for the FKH domain of FoxP1 obtained from replica exchange discrete molecule dynamics (rxDMD) simulations. The potential mean force plot of the *R*g vs. α-helix content was obtained at 300 K, showing the representative structures for the folded and disordered monomer.

(D) The sm-2D plots for the same FRET variants as in (A) but in dimeric conditions. The dimer was obtained by incubating the labeled monomer with a saturating concentration of the unlabeled monomer. The lines and FRET states are indicated as in (A). The representative dimeric structure of the HF state is shown.

(E) sm-2D plots for the fluorescence anisotropy analysis of the monomer and dimer variants C18, C57, and C78, indicating the Perrin line of high (in dark gray, folded) and low (in light gray, disordered) populations, in accordance with the lifetime fit (material and methods). The respective populations predicted by PDA analysis are shown at the time window of 3 ms. According to the fit to a dynamic two-state equilibrium (material and methods), the dynamic line (in orange) and the relative contribution of each state (Rigid, folded; Flexible, disordered) is shown for all variants.

additional population with an FRET efficiency of ~0.85, defined as high FRET (HF) (Figure 2B). These populations coincide with the lifetime-based FRET analysis of the molecules; therefore, we refer to them as HF and LF. The D-A distance extracted from this high FRET value (~38 Å) is similar to that expected in the folded monomer (Figure S1). Therefore, the lack of an HF population in the C18-C78 variant could indicate the absence of the folded state or a fast folded to disordered transition. To explore these possibilities, we plotted the FRET efficiency against the observation time (Figure S2). For short observation times, we found broad FRET efficiency

distributions reaching the HF state. For long observation times, we mainly observed low FRET efficiencies. This observation indicates that C18-C78 HF and LF are in fast exchange compared with the observation time, i.e., the diffusion time. The LF population has a long D-A distance. Thus, LF can be interpreted as an expanded and likely disordered chain. These observations are consistent with the previously found disordered intermediate on the 3D-DS dimerization pathway.[17,24]

To compare and discriminate which FRET models best describe our observations, we computed FRET lines (Figure 2A, material and methods). An FRET line is a parametric relationship between FRET observables computed by varying model parameters.[34,35] We first compute the static FRET line (red line in Figure 2B) that describes molecules not undergoing conformational changes. The 2D histograms do not match this model. Thus, single molecules must change their FRET state while observed.[34,35] We also considered the case of a disordered population, testing the data to a worm-like chain (WLC) line that depicts the FRET variation just as the flexibility changes in a disordered chain (black line).[34,35] The LF population is located on the WLC line, although the WLC line does not track the high FRET population. Finally, we added an FRET line describing a dynamic exchange between the HF and disordered (LF) states (Figure 2B, orange line). This line nicely follows the experimental data, supporting that the monomeric FKH is in dynamic equilibrium between a folded state and an extended disordered ensemble on the duration of a single-molecule event.

Since the fluorescence data suggested that most of the monomeric FKH molecules in FoxP1 behave as disordered, we used replica exchange discrete molecular dynamic (rxDMD, details in material and methods) simulations over a temperature range of 280–370 K (Figure 2C) as a tool to explore this behavior in detail. rxDMD is known for its ability to sample the conformational energy landscape, including predicting order-to-disorder transitions, folding, and other relevant structural dynamics phenomena, as demonstrated in previous studies.[38–40]

To assess the structural behavior of the monomer, we computed the potential mean force as a function of the radius of gyration (R_g) and the α-helical content of FKH (Figure 2C). We chose 300 K (Figure 2C) because this temperature is lower than the computed T_m (Figure 2C). Our simulations revealed that the FKH domain has no defined energy minimum corresponding to its native fold. Instead, it can populate a continuum of configurations from folded (containing the expected α-helical content) to disordered states with low α-helical content. Furthermore, we observed that the loss of α-helix content does not result in significant changes in the R_g until the protein reaches an extended unfolded state, by which the R_g value was ~45 Å (Figure 2C).

We then compared the information obtained from rxDMD with the WLC model used to describe the LF population of the monomers in the sm-2D graphs, considering the respective equation to extract the R_g from the lifetime FRET-derived analysis[41] (material and methods), in accordance with that described in Hofmann et al.[42] The values of R_g computed were 42 and 53 Å for the C57-C78 and C18-C78, respectively (Table S2), which includes the length of the dyes. Additionally, we used the CALVADOS2 server[43,44] to compute the R_g of both FRET variants considering them as disordered chains. The value computed for the C57-C78 region was 13 Å, whereas for the region C18-C78 was 45 Å. We had a good agreement between FRET-derived and the predicted R_g for the region C18-C78, but the FRET-derived R_g of the C57-C78 region is significantly higher than the predicted one. However, this is still possible considering the extended chain length (L_C) (Table S3).

Overall, the combination of experimental and computational evidence suggests that the monomeric FKH domain actively explores multiple disordered configurations even at physiological temperatures, corroborating its propensity for disorder.[17]

A cooperative stabilization of the FKH domain via dimerization through 3D-DS

After characterizing the disordered nature of the monomeric FKH, we sought to investigate the impact of 3D-DS dimerization on the structural dynamics of the FKH domain. To this end, we prepared dimers using pM concentration of FRET-labeled samples (C18-C78 or C57-C78) saturated with 500 nM of unlabeled wild-type (WT) protein. By adding excess of unlabeled WT protein and considering the dissociation constant determined for each single-cysteine variant,[17] we ensured the accumulation of dimeric species containing only one labeled monomer (C18-C78 or C57-C78) (Figure 2D and Figure S3). We repeated the measurements and data processing described for monomers (Figure 2B) and observed that the dimers also exhibited a dynamic equilibrium between the folded and disordered ensembles (Figure 2D). However, the dimers displayed a significantly higher proportion of the folded population (high FRET values) than the monomers (Figures 2A and 2C).

We wanted to determine if the stabilizing effect of dimerization is cooperative despite observing significant differences in the FRET distributions among the two variants (Figure 2D). Thus, we used single-molecule fluorescence anisotropy (smFA) as a screening approach to monitor the single-cysteine variants evaluated in FRET experiments (C18, C57, and C78). For smFA, we labeled the proteins with BODIPY FL, as this dye is closer to the protein's backbone and, therefore, more sensitive to the local flexibility of the backbone compared with the Alexa dyes.[37,41,45] In smFA, we excited single molecules using polarized excitation and collected the fluorescence emission into parallel and perpendicular polarized detectors. We then analyzed the fluorescence decay from each single-molecule event to obtain the average lifetimes and fluorescence anisotropies (Figure 2E and Table S4).

From the fluorescence anisotropy decays, we considered two different states with their corresponding rotational correlation times (ρ) (See data analysis). We successfully fitted all samples with this model (Table S3), finding a fraction with a low average anisotropy (r_G) between ~0.02–0.06 (high flexibility) and a high r_G between ~0.1–0.3 (low flexibility) (Figure 2E and Figure S4). Moreover, the measured samples displayed broad distributions between the calculated anisotropy lines, although in general the low anisotropy populations seem to be more favored. We interpreted this behavior as a dynamic exchange between conformations. This is best described by the theoretical dynamic anisotropy line computed (orange line in Figure 2E, material and methods).

We later investigated if the low and high flexibility populations in the monomer are effectively displaying dynamic exchange along the observation time. To determine the kinetics, we analyzed the intensity-based anisotropy using a two-state rigid-flexible equilibrium, resolving the dynamics at timescales comparable to the diffusion time by employing the probability distribution analysis (PDA) algorithm.[46–48] All anisotropy distributions showed better χ_r^2 values when globally fitting all time windows with a kinetic model (Table S5), corroborating the visual inspection (Figure 2E).

When examining the monomer, we observed that helices *H*3 (C57) and *H*5 (C78) display a high fraction of low anisotropy or high backbone flexibility, while the helix *H*1 (C18) behaved more rigidly with higher anisotropy (Figure 2E). Upon dimerization, the populations are still better fitted when including dynamics (Table S5), but

CellPress
OPEN ACCESS

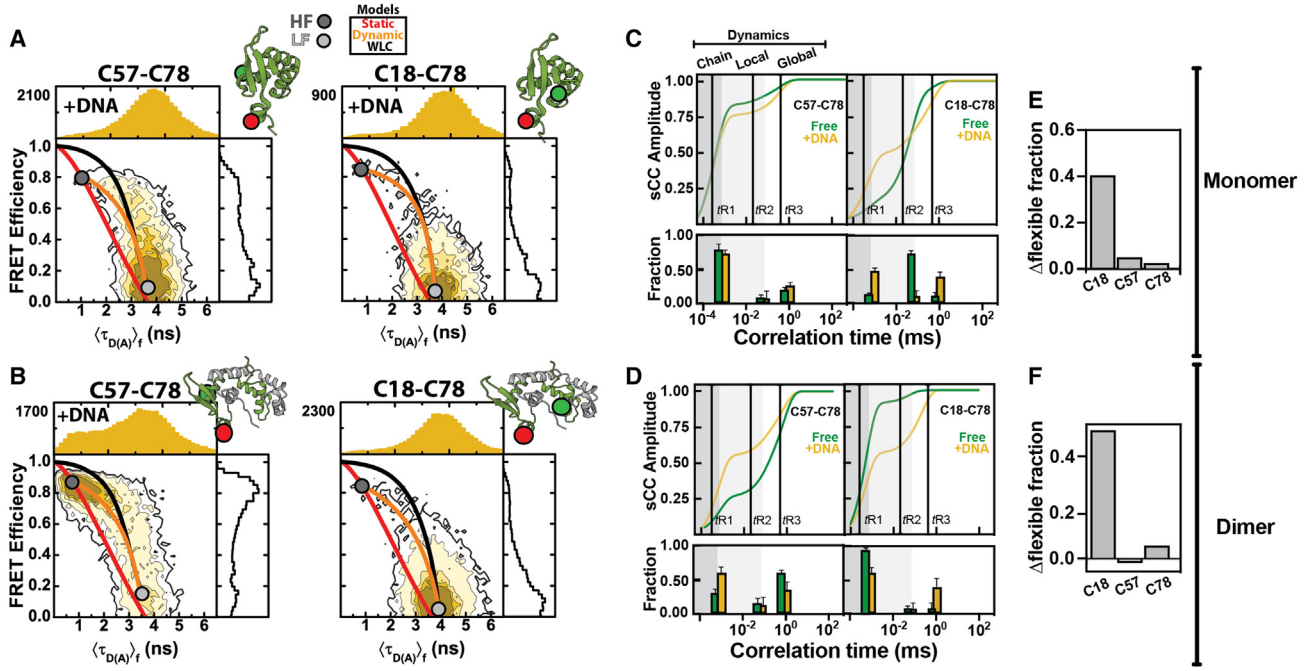

Figure 3. Structural dynamics of the monomeric and dimer FoxP1 FKH in the presence of DNA

(A and B) Single-molecule multiparameter fluorescence spectroscopy sm-2D histograms of the FRET efficiency and the average fluorescence lifetime of the donor in the presence of acceptor $\langle\tau_{D(A)}\rangle_f$ for the monomer (A) and the dimer (B) FRET variants. The DNA used was 1.5-fold higher than the total protein in each scenario (monomer: ~pM labeled protein+100 nM unlabeled protein; dimer: ~pM labeled protein+500 nM unlabeled protein). Each FRET state is shown as a filled circle (HF in dark gray circle, LF in light gray circle). The representative structure for the HF state with the monitored region by the FRET pair (donor, green; acceptor, red) is shown. The three physical FRET models (static, WLC, and dynamic) are represented as lines in the sm-2D. Correction parameters are found in Table S2. The FRET efficiency of the free protein is shown for comparison.

(C and D) Determination of the dynamic transitions between low and high FRET species using filtered FCS (fFCS) for the monomers (C) and dimers (D). Each loss of amplitude in the respective species cross-correlation (sCC) vs. correlation time is related to an FRET exchange. For each FRET variant in the absence (green) and presence (yellow) of DNA, different conformational transitions are described by specific relaxation time (t_R). From the cross-correlation curves, the amplitude of each t_R component is extracted (material and methods).

(E and F) Difference between the flexible contribution in the variants C18, C57, and C78 in the monomer (E) and dimer (F) in the presence and absence of DNA (Δflexible = presence-absence of DNA). A higher Δflexible, a higher increase in backbone's flexibility.

with a global increase in the backbone rigidity, supporting the idea that the 3D-DS leads to a cooperative accumulation of the folded state of the protein.

DNA binding differentially perturbs the monomeric and dimeric states of the FKH domain

To understand the impact of DNA binding on the monomeric and dimeric states of the FKH domain, we repeated the single-molecule experiments using the FRET variants C57-C78 and C18-C78 in the presence of DNA. We first established the conditions in which DNA binds to the monomeric and dimeric states of the FRET variants (Figure S3). Next, we examined the FRET variants bound to DNA in their monomeric state. We observed an increase in the HF population (Figure 3A) compared to when it is unbound. This effect was more pronounced in the C57-C78 variant than in the C18-C78 variant (Figure 3A). Comparing the static, WLC, and dynamic FRET models described by the red, black, and orange lines revealed that the folded and disordered states are in dynamic equilibrium.

Oppositely, the presence of the DNA decreases the HF population in the dimer of the FRET variants compared with its unbound form. We observed an increase in the LF populations (Figure 3B). This observation indicates that DNA stabilizes the folded monomer but destabilizes the 3D-DS dimer.

Next, we investigated the effect of DNA on the dynamic equilibrium between the folded and disordered states of both monomeric and dimeric FRET variants. First, we used the burst variance analysis (BVA)[49] to determine the heterogeneity of the FRET populations, comparing the excess variance of the FRET efficiency (S^2) segments of different m-photon numbers (see materials and methods). To compare the FRET variants, we computed the excess of the variance up to the timescale comparable to the diffusion time.

In both the absence and presence of DNA, both the monomer and dimer exhibit significant variability among the FRET populations, as depicted in Figures S5 and S6. This variability supports the notion of heterogeneity along the protein chain. By analyzing the average excess of variance in the variants, we observed a decay that indicates a reduction in dynamics reaching equilibrium within the low millisecond timescale (Figures S5 and S6). Generally, the presence of DNA decreases the heterogeneity of the monomers but has the opposite effect on the dimer (Figures S5 and S6). However, it does not notably influence the decay pattern. We speculate that the observed high heterogeneity might correspond to disordered dynamics, while the variance decay could signify a kinetic transition between HF and LF states.

Considering the heterogeneous behavior described by BVA, we tried to resolve the kinetic transition between the FRET states using a simplified two-state HF $\rightleftarrows$ LF equilibrium model to analyze the intensity distribution of the FRET signals, resolving dynamics at timescales comparable to the diffusion time. We employed the PDA algorithm,[46–48] as it has shown to solve more quantitatively the kinetic transitions.[35]

We globally fit the intensity data for different time windows around the diffusion time (Δt = 1, 3, and 10 ms) and compared it with a static (non-exchanging) and a dynamic (exchanging) two-state model. We observed a significant improvement in the model's goodness (χ_r^2) in the dynamic model than in the static model (Table S6), obtaining also kinetic rates that are in accordance with the variance decay showed in BVA. However, the χ_r^2 values suggest the need for a more complex model.

In that line, we sought to investigate if additional transitions were occurring at faster timescales than the diffusion time, increasing the model's complexity. To accomplish this, we utilized fFCS (Figure 1B),[50,51] allowing us to examine the dynamic spectrum of exchange processes from hundreds of nanoseconds to tens of milliseconds. fFCS is helpful for this purpose since it takes advantage of the fact that the intensity fluctuations due to specific FRET states can be correlated on these timescales.

We globally analyzed the fFCS (species autocorrelation and cross-correlation) curves for both FRET variants (C57-C78 and C18-C78) in monomeric (Figure 3C) and dimeric conditions (Figure 3D) in the absence and presence of DNA (Table S7). For the C57-C78 FRET variant, we observed that an FRET transition around nanoseconds (t_{R1}) is dominant in the monomeric conditions, even in the presence of DNA (Figure 3C). Therefore, we interpreted it as the conformational sampling of the disordered state, which must occur at sub microseconds.[52] In contrast, for the C18-C78 variant, we found that a dominant FRET transition around microseconds (t_{R2}) is distributed homogeneously between fast and slow timescales (Figure 3C). Thus, the structural transitions of the FKH domain are complexes and differentially modulated by the DNA.

The behavior of the dimers differs significantly (Figure 3D). In the case of the C57-C78 variant, the slow exchange dominates (t_{R3}), reflecting transitions between the

folded and disordered states. On the other hand, for the C18-C78 variant, which represents changes in helices *H*1-*H*5, the fast transition (t_{R1}) dominates. When bound to DNA, the impact is propagated differently across the backbone, but the disordered contribution accounts for approximately 50% of the total dynamics in both variants. The observed timescales indicate that the DNA fine-tunes the structural dynamics, as evidenced by an increase in disorder behavior in the C57-C78 variant but a decrease in this behavior in the C18-C78 variant (Figure 3D).

We then performed single-molecule anisotropy measurements in both monomer and dimer conditions to investigate the local impact of DNA (Figures 3E and 3F). We analyzed fluorescence anisotropy and extracted the dynamics as previously described for the monomers (Figure 2E). In this case, two anisotropy states with a dynamic exchange were necessary to globally fit multiple time windows. We compared the flexible behavior of the protein in the absence and presence of DNA (Figures 3E and 3F). In general, DNA increases FKH's flexibility by an increase in the contribution to the low anisotropy, except when the dye is located in helix *H*3 in dimer conditions, suggesting that DNA destabilizes the protein's backbone (Figures 3E and 3F). However, for the dimer, we observed a higher increase in flexibility of helices *H*1 and *H*5, which can explain the favoring of the disordered low FRET state compared with the monomer.

DNA binding controls the dimerization of the FKH domain

Based on our findings, binding to DNA significantly impacts the folded state of FoxP1 FKH, increasing the protein structural disorder, which may affect its dimerization equilibrium.

To explore the impact of the DNA binding on the 3D-DS dimerization, we developed a dimerization assay using a BODIPY FL-labeled single-cysteine variant of FoxP1 to track the kinetics of the dimer formation by measuring steady-state anisotropy. To assess the impact of DNA binding, we monitored changes in fluorescence anisotropy upon the binding of the unlabeled R53H variant of FoxP1, which has an affinity to DNA over 20 times lower than the WT protein (Figure S7). In this scenario, the labeled monomer is the only component affected by the presence of DNA due to the low R53H ability to bind the DNA in the concentration range used. In the absence of DNA, the anisotropy of the labeled FoxP1 increases with the presence of the FKH variant R53H, indicating the association between monomers (Figure 4A). We repeated the experiment using different concentrations of the R53H variant. We observed that the maximum FoxP1 anisotropy increased as a function of the concentration of the R53H variant (Figure 4B), indicating protein association. We fitted the curves with a single exponential under pseudo-first-order conditions to calculate the observed rate constant (k_{obs}) as a function of the R53H variant concentration (materials and methods), from which we extracted the association (k_{ass}) and dissociation (k_{diss}) rate constants (Figure 4C and Table S8).

Our results indicate that the dimerization process may be constrained by the order-to-disorder transition required to form the 3D-DS dimer (Figure 2). The slow association rate observed without DNA ($6 \pm 0.4 \cdot 10^4$ M^{-1} min^{-1}) supports this hypothesis. When the labeled protein was preincubated with DNA at a protein:DNA stoichiometry of 2:1, the k_{ass} value decreased by approximately 70% (Figure 4C and Table S8). Furthermore, by analyzing the effect of DNA concentration on the association, we found that the k_{obs} value decreased proportionally to the increase in DNA concentration, confirming that binding to DNA in monomeric conditions prevents dimerization (Figure 4C inset). As a result, the structural changes induced by DNA binding increase the accumulation of the disordered ensemble and shift the dimerization equilibrium toward the monomeric state. Then, the DNA-monomer complex acts

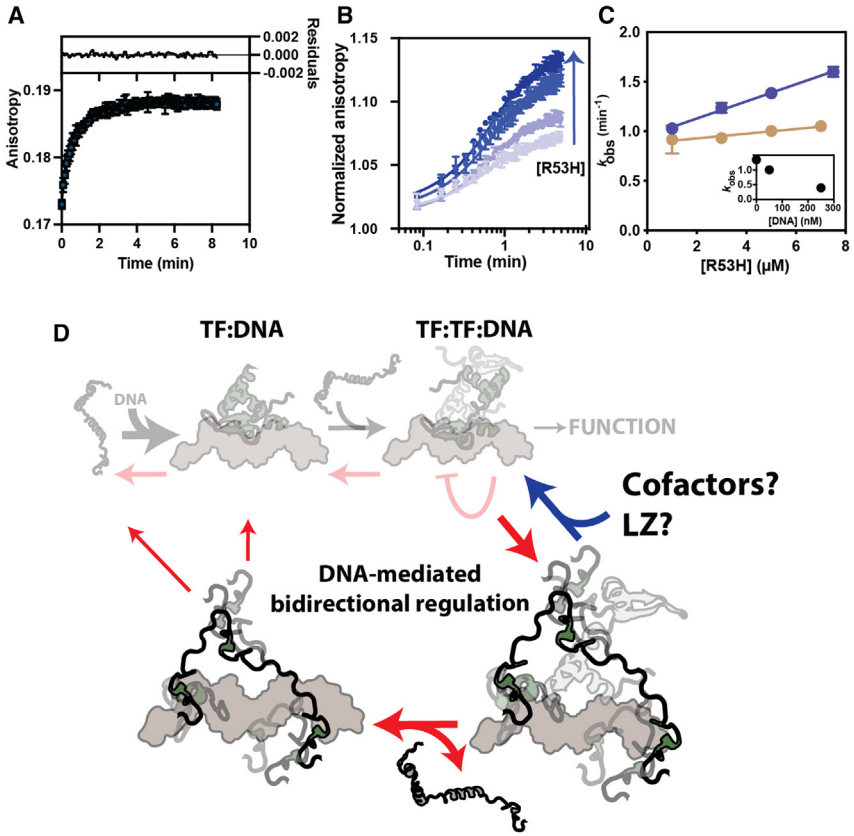

Figure 4. DNA acts as a negative regulator over the dimerization of FoxP1

(A) Changes in anisotropy of labeled FoxP1 (100 nM) upon the addition of 3 μM of unlabeled R53H variant. The kinetic change of the signal was fitted to a single exponential curve, showing the corresponding residuals.

(B) The same experiment as (A) but titrating with increasing concentrations of the R53H variant. The concentration of the labeled protein was 100 nM, whereas the unlabeled R53H at 1 (light purple), 3 (purple), 5 (light blue), and 7 μM (blue) was used.

(C) Comparison of observed association rate constant (k_{obs}) in (A) in the absence (blue) and presence (brown) of 50 nM of unlabeled DNA. The assay in the presence of DNA was as follows: in a preformed FKH(FoxP1):DNA complex at stoichiometry 2:1, and we monitored the 3D-DS:DNA formation upon the increasing concentration of the unlabeled R53H. Inset: comparison of the k_{obs} by titrating with 3 μM of R53H in preformed FKH:DNA complexes 100 nM:0 nM, 100 nM:50 nM, or 100 nM:250 nM.

(D) Schematic structural and monomer-dimer equilibrium in the absence and presence of DNA to highlight the reversible regulation over the FoxP function. Each state (monomer and dimer) bound to DNA was described as dynamically exchanging between the folded and a disordered state. We qualitatively estimated the equilibrium transitions between them by their relative contribution in the sm-2D plots. The red arrows correspond to the direction of the reverse process, and the thickness corresponds to the impact exerted by the DNA. The blue arrow shows the proposed role of regulatory proteins (such as cofactors) and the additional domains of FoxP1 (as the LZ domain).

as a negative allosteric control over dimerization by increasing the energy barrier for dimerization.

DISCUSSION

The interaction between TFs and DNA is one of the most relevant phenomena within a cell, and usually the adoption of the complex induces structural changes in the TFs. However, the precise role of DNA in the stability of the complex and the mechanisms by which it is modulated remain poorly understood.

We used the FoxP1 DNA-binding domain to investigate the dynamic and structural response of TFs when bound to DNA, both in monomeric and dimeric states. These TFs play a significant role in neural and embryonic development and speech, language, and immune disorders,[16,53] and they are able to bind DNA as monomers[21,54] and also form 3D-DS dimers through a process known as 3DS-DS dimerization,[18] which it has been argued as their active form.[18,25,26] The multiple binding phenomena around the activity of FoxP proteins point to a revision of the prevailing notion of the unidirectional TF:DNA→TF:TF:DNA mechanism, where DNA induces the folding and subsequent association of TFs required for function (Figure 1A), to a more complex model where the TFs:DNA complex duration is mediated by the TF's dynamics exerted by the DNA itself. Hence, understanding the regulatory mechanisms governing TF:DNA formation is necessary to fully capture the dynamic nature of the binding equilibriums of the multiple complexes.

Our study revealed how DNA cooperatively modulates TF dimerization, particularly the 3D-DS dimerization. Our experimental and computational approaches revealed that the FKH domain exchanges between folded and disordered states at physiological temperatures. Surprisingly, we found that DNA binding slightly modified the structural dynamics and behavior of the monomer when bound to DNA (Figure 3), highlighting the intrinsically disordered nature of the complex.

However, the behavior seems not to be homogenously distributed among the chain. For example, the calculated radius of gyration (R_g) of the FRET variant C57-C78 of the low FRET state is significantly higher than the prediction from CALVADOS2, suggesting either a more extended region or an artifact related to the position of the dyes or another structured conformation that cannot be simply explained with our results. To explore possible artifacts, we included the information of the dyes to our simulations to calculate the average interdye distance between positions 57 and 78 in the disordered conformation, obtaining an average value of ~68 Å (Figure S8). Only considering an uncertainty of 7% in the orientation factor (κ^2),[30,31] we extrapolated an FRET efficiency of 0.15 [0.1–0.21], where brackets represent confidence interval, which is similar to the experimental value obtained in our work. Despite our discrepancies, the low FRET state behaves effectively with high flexibility and heterogeneity, as consistently observed in anisotropy, BVA, PDA, and more importantly, fFCS.

In addition, we found that dimerization enhances the stability and folded state of FoxP1, as observed in smFRET, fFCS, and anisotropy experiments, but DNA binding cooperatively uncouples the folded state and promotes the accumulation of the hypothetical disordered protein:DNA complex, favoring the dimer's dissociation (Figure 4D). The 3D-DS dimer is commonly accepted to be the functional state of FoxP proteins,[17,18,20,21,25,55,56] enabling the chromosomal tethering and executing their repression role. Moreover, several disease-causing mutations on the FKH affecting the dimerization ability highlight the functional relevance of the adoption of the dimer in the cellular context.[28,57]

This disorder-promoting effect of the DNA on the FoxP1 dimer introduces the role of the DNA as a co-regulator of the transcriptional activity of TFs, expanding from a unidirectional model to an unexplored reversible mechanism in transcription factors, where the DNA triggers a response and modulates the protein's dimeric state by inducing disorder (Figure 4D). This mechanism could act opposite to the "folding-upon-binding," affecting the repression function of human FoxP proteins by reducing the prevalence of the functional-dimeric state.

Based on our findings, we propose that the chromosomal tethering described *in vivo*[18] may depend on additional components, including the presence of (1) other domains (such as LZ) on this family of TFs; (2) additional protein partners such as NFAT (nuclear factor of activated T-cells),[20,25] Runt-related transcription factors (RUNX),[58] and CtBP1 (C-terminal binding protein 1); (3) different post-translational modifications[59]; and (4) the heterogeneity of the protein composition in the nucleus, as observed in membrane-less organelles.[60–62] These additional cofactors may promote the folding of the dimer when bound to DNA. This dynamic modulation of stability of the protein-DNA complexes may have an impact on the transcriptional activity of FoxP proteins, and therefore crucial for maintaining transcriptional equilibrium for homodimeric and heterodimeric 3D-DS species complexes that bind to different DNA sequences. For the case of the heterodimer FoxP1-FoxP2, the changes in the FoxP1's dynamics induced by the DNA favor the protein:protein association,[19] highlighting the versatile role of the ligand in the structural and functional properties of the protein, by which the differences in the protein's flexibility in the absence or presence of DNA could guide the acquisition of a homo- or hetero-dimeric complex.

Therefore, a more complete model is required to fully describe the structural modulation of human FoxP1's function, presenting us with the challenge of unraveling the features of inter-domain and inter-protein communication within the FoxP subfamily, which enable them to function as master regulatory TFs.

EXPERIMENTAL PROCEDURES

Resource availability

Lead contact

Further information and requests for resources and reagents should be directed to and will be fulfilled by the lead contact, Hugo Sanabria (hsanabr@clemson.edu).

Materials availability

The recombinant constructs developed in this work will be available upon request.

Data and code availability

Code availability. This article does not contain any new code.

Data availability. Datasets from confocal smMFD (Raw, MFD Bursts, time-correlated single-photon counting [TCSPC], PDA, and FCS), along with biochemical data generated, are available upon request from the lead contact. This work did not generate any new accession code for the data.

Protein expression and purification

The WT forkhead domain of the human FoxP1 and its variants (L18C, S57C, and V78C) were cloned into a modified pET-28a vector containing a His6-tag, a TEV cleavage site, and an S-tag sequence toward the 5′ end of the gene. The plasmid containing FoxP1 variants was created by PCR mutagenesis using the QuickChange Site-directed mutagenesis kit (Stratagene, La Jolla, CA, USA). We transformed *E. coli* C41 cells (Invitrogen) with the pET28a vector to overexpress the FoxP1 protein. Protein expression was induced by 0.5 mM IPTG followed by overnight incubation at 15°C to attain the optical density at A600 in the range of 1.4–1.6. Further, proteins were purified using Ni^{2+}-NTA affinity chromatography as described previously.[17]

Labeling of FoxP1

Three dual-cysteine variants (L18C, S57C, and V78C) were expressed and purified for dual labeling with fluorescent dyes. Prior to labeling, 100 μM FoxP1 was added

to buffer A (20 mM HEPES, pH 7.8, 150 mM NaCl, 2 M GdmCl) with 0.5 mM Tris (2-carboxyethyl) phosphine hydrochloride (TCEP) and incubated over 30 min at room temperature. Next, we buffer exchanged by adding 500 μL of 100 μM FoxP1 with 2 mL buffer A to the PD 10 column and further concentrated. The eluted protein was labeled with Alexa 488 by adding one-third of cysteine concentrations in the protein and incubated for 2 h at room temperature. Next, buffer exchange occurs as discussed earlier.[17] Alexa 647 was added double the cysteine concentration in the protein and incubated overnight at 4°C. We carried out a buffer exchange the next day and measured the dual-labeled protein concentration. Finally, excess free fluorescent dyes were removed by size exclusion chromatography.

Size exclusion chromatography

FoxP1-labeled monomer protein is separated from dimer and free dye using an FPLC system with Superdex 75 column (Bio-Rad). First, the column was equilibrated with 50 mL of standard buffer (20 mM HEPES pH 7.8, 150 mM NaCl) at 4°C. Next, the FoxP1 monomer is eluted within one column volume using the same buffer. The collected fractions were stored at 4°C for the experiments.

smMFS

For single-molecule multiparameter fluorescence detection (smMFD), ~100 pM labeled samples were diluted in standard buffer (20 mM HEPES, 150 mM NaCl, pH 7.8) in the presence of 500 nM unlabeled protein. For smMFD, we used a 500-μL sample volume containing NUNC chambers (Lab-Tek, Thermo Scientific, Germany). The instrument response function was determined by measuring water, standard buffer for background subtraction, Rhodamine 110 for green, and Rhodamine 101 for red channels for calibrations were used. The detection efficiency was calibrated with a mixed solution of known distance separation between donor and acceptor dyes containing dual-labeled DNA oligonucleotides as previously described.[17]

smMFD was carried out using diode lasers at 485 nm (LDH-D-C 485 PicoQuant, Germany, power at objective 110 μW) and at 640 nm (LDH-D-C 640 PicoQuant, Germany, power objective 60 μW), operating at 40 MHz in PIE mode. The freely diffused molecules excited and passed through a 60X detection volume, and the emitted fluorescence signal was collected with a 70-μm pinhole using a 1.2 NA collar (0.17) corrected Olympus objective. The green and red color signals were used through bandpass filters HQ 520/35 and HQ 720/150, respectively, and these channels are further divided into parallel and perpendicular components. Two detectors were used for each spectral window (e.g., green and red channels). Four synchronized input channels and a TCSPC module (HydraHarp 400, PicoQuant, Germany) were used for data registration. Sub-ensemble time-resolved fluorescence data were collected as described previously.[17,38,63]

Anisotropy measurements

BODIPY-labeled single-cysteine variants (L18C, S57C, and V78C) were measured as described in the smMFS approach. Before data collection, the sample chamber was treated with 0.01% of tween 20 to avoid adsorption. Samples were measured with 100 p.m. BODIPY-labeled FoxP1 monomer and 100 nM unlabeled FoxP1 using standard buffer (20 mM HEPES pH 7.8, 20 mM NaCl). BODIPY-labeled dimers were prepared by adding 500 times of unlabeled WT FoxP1 to labeled FoxP1, followed by 2M guanidine HCl. Proteins were mixed, and the buffer was exchanged with a standard buffer. The sample was concentrated and incubated at 37°C for 30 min. The DNA samples were titrated separately with monomers and dimers. Prior to titration,

labeled proteins were prepared separately, as discussed previously. An amount of 500 nM labeled FoxP1 was titrated with four times of DNA and incubated at room temperature for over 10 min. The final concentration for the anisotropy measurements was 100 p.m. of labeled protein. We measured 2 nM Rhodamine 110 in water to calculate the G factor.

Ensemble measurements to follow the WT FoxP1:R53H FoxP1 association were performed in a Jasco FP-8300 spectrofluorometer with polarized filters. The C57 variant of FoxP1 labeled with BODIPY FL was titrated with 1, 3, 5, and 7 μM of unlabeled R53H variant of FoxP1. The association was monitored by following anisotropy changes at 37°C. For association kinetics in the presence of DNA, different labeled FoxP1:DNA ratios were incubated with 3 μM of R53H variant, and a sample containing 100 nM:50nM ratio FoxP1:DNA was titrated as performed in the absence of DNA to determine the association and dissociation rates. G factor was measured using free dye at 200 nM concentration.

All the dimerization reactions were fitted into a single exponential curve, where the observed rate represents a pseudo-first-order reaction, considering that the unlabeled R53H variant is in excess of the labeled C57-BODIPY variant. In that scenario, the true association (k_{ass}) and dissociation (k_{diss}) are obtained from Equation 1 and depend on the concentration of the unlabeled protein used in homo and heterodimerization:

$$k_{obs} = (k_{ass} \cdot [FoxP]) + k_{diss} \quad \text{(Eqaution 1)}$$

Fitting procedures were performed using the software GraphPad Prism 8.0 (www.graphpad.com).

Anisotropy lines

For each burst, we determine the steady-state anisotropy, r_S, the fluorescence weighted average lifetime, τ_F, and compute two-dimensional frequency histograms referred to as anisotropy histogram. Analogous to FRET-lines[34,35] that describe populations of single molecules on multidimensional FRET efficiency histograms, we describe populations on the anisotropy histograms by parametric relations. The relation between r_S and τ_F parameterized by a parameter ν an anisotropy line.

$$r_S(\nu) = F^{-1} \int t \cdot r(t|\nu) dt \quad \text{(Equation 2)}$$

$$\tau_F(\nu) = F^{-1} \int t \cdot f(t|\nu) dt \quad \text{(Equation 3)}$$

Here, $f(t)$ and $r(t)$ are the time-resolved fluorescence and anisotropy decay, respectively, and $F = \int f(t|\nu) dt$ is the total fluorescence intensity.

There are many possibilities to define an anisotropy line. The most common anisotropy line is defined by parameters such as the rotational correlation time, ρ_i, and the population x_i of fluorophores in state i. For a single state with a rotational correlation time ρ, the integral steady-state anisotropy, r_S, and the fundamental anisotropy r_0 are related by the Perrin equation[64]

$$r_S = \frac{r_0}{1+\tau_F/\rho}, \quad \text{(Equation 4)}$$

that is obtained by solving the integral for $r(t|\nu = \rho) = r_0 e^{-t/\rho}$. For N states that are in fast exchange with distinct rotational correlation times, this becomes

$$r_S(\tau_F) = r_0 \sum_{i=1}^{N} \frac{b_i}{1+\tau/\rho_i} \quad \text{(Equation 5)}$$

In the case of two states with different rotational correlation times that are in slow exchange, r_S is not fully averaged.

For each burst, we determine the steady-state anisotropy, r_S, the fluorescence weighted average lifetime, τ_F, and compute two-dimensional frequency histograms referred to as anisotropy histogram. Analogous to FRET-lines[34,35] that describe populations of single molecules on multidimensional FRET efficiency histograms, we describe populations on the anisotropy histograms by parametric relations. The relation between r_S and τ_F parameterized by a parameter ν an anisotropy line.

Anisotropy lines extend on the concept of FRET lines by considering the rotational relaxation time, ρ, and the fundamental anisotropy, r_0, in addition to the radiative rate constant k_F, and the fluorescence lifetime τ that are needed for computing FRET lines. Briefly, an anisotropy line is a parametric relation between an experimental fluorescence anisotropy measure (e.g., the steady-state anisotropy, r) and another measure (e.g., the fluorescence weighted average lifetime, $\langle\tau_D\rangle_F$). Anisotropy lines are computed as follows. First, experimental observables (e.g., r and $\langle\tau_D\rangle_F$) are computed for a set of parameters. Next, the parameters determining the experimental observables (e.g., FRET rate constants) are varied, and resulting observables are tabulated. Alternatively, observables are related by an analytical expression. We compute anisotropy lines for $\langle\tau_D\rangle_F$ and r. In our single-molecule experiments, r was determined using the integrated background corrected fluorescence intensities of the parallel F_p and perpendicular F_s detection channel

$$r = \frac{F_p - F_s}{F_p+2GF_S} \quad \text{(Equation 6)}$$

where G is a factor correcting for differences in the detection efficiency of the p and s channel. For parameterizing a relation between r and $\langle\tau_D\rangle_F$, we define a set of states, $\{\Lambda_k\}$. Each state Λ_k, is defined by a fluorescence lifetime, τ_k, a rotational relaxation time, ρ_k, and its population fraction x_k. The fluorescence decay of Λ_k in the p and s detection channel is

$$f_{p,k} = \frac{1}{3} f_k(1 + 2Gr_k) \quad \text{(Equation 7a)}$$

$$f_{s,k} = \frac{1}{3} f_k(1 - r_k) \quad \text{(Equation 7b)}$$

where the fluorescence decay $f_k = k_F e^{-\frac{t}{\tau_k}}$ and the anisotropy decay $r_k = r_0 e^{-\frac{t}{\rho_i}}$. Hence, r of a set of states, $\{\Lambda_k\}$, is

$$r(\{\Lambda_k\}) = \frac{\int_{t=0}^{\infty} \sum_k x_k f_k r_k dt}{\int_{t=0}^{\infty} \sum_k x_k f_k} = r_0 \frac{\sum_k x_k \tau_k \rho_k (\rho_k+\tau_k)^{-1}}{\sum_k x_k \tau_k}. \quad \text{(Equation 8)}$$

The corresponding fluorescence weighted average lifetime $\langle\tau_D\rangle_F$ is

$$\langle\tau_D\rangle_F(\{\Lambda_k\}) = \frac{\sum_k x_k \tau_k^2}{\sum_k x_k \tau}. \quad \text{(Equation 9)}$$

If all $\{\Lambda_k\}$ that shares a single fluorescence lifetime and rotational correlation time

$$r = r_0 \frac{\rho}{\rho+\tau}. \quad \text{(Equation 10)}$$

This relation, that is also known as Perrin equation, is a "static" anisotropy line, as it is valid for all "pure" states that have a single rotational time ρ and lifetime τ. In cases where a single fluorescence lifetime has had multiple rotational relation times

$$r = r_0 \sum_{k=1}^{K} x_k \frac{\rho_k}{\rho_k + \tau} \quad \text{(Equation 11)}$$

Even though such case describes multiple rotational states, we still refer to these lines as static anisotropy lines, as they can describe single FRET states of flexible coupled dyes.[65]

Dynamic anisotropy lines describe the exchange/mixing of states. For a two-state system $\{\Lambda_1, \Lambda_2\}$ $x_1 = \tau_2(\tau_F - \tau_2)/(\tau_1 - \tau_2)(\tau_1 + \tau_2 - \langle\tau\rangle_F)$. Thus, $r(\tau_F|\{\Lambda_1, \Lambda_2\})$, the dynamic anisotropy line that describes the Λ_1/Λ_2 mixing, is a linear in τ_F

$$r(\tau_F|\{\Lambda_1, \Lambda_2\}) = \frac{r_0}{\tau_1 - \tau_2}\left(\tau_F\left(\frac{\rho_1(\rho_2+\tau_2) - \rho_2(\rho_1+\tau_1)}{(\rho_1+\tau_1)(\rho_2+\tau_2)}\right) + \frac{\tau_1\rho_2(\rho_1+\tau_1) - \tau_2\rho_1(\rho_2+\tau_2)}{(\rho_1+\tau_1)(\rho_2+\tau_2)}\right) \quad \text{(Equation 12)}$$

and connects the "static" anisotropy lines of Λ_1 and Λ_2 by a straight line (see Figure 2 in the main text).

Discrete molecular dynamics simulations

Interatomic forces in all-atom molecular dynamics simulations were used to run the discrete molecular dynamics (DMD). Medusa force field with discretized potentials and implicit solvent were used to run DMD simulations. As described earlier, the implicit solvent model used in DMD was a CHARMM19-based energy function and Gaussian solvent-exclusion model.[38,39,41] As previously described, the FKH structures were generated by homology modeling.[17] For FoxP1, we used the DMD software package to run all-atom replica exchange simulations. Initial equilibration was run with 50 ns each with ~2fs time step. A total of 18 replicas for each protein were allowed to exchange between 18 temperature baths equally spaced between 275 K and 350 K. The total simulation time for each replica is ~1 μs. Analysis of the trajectories was performed using VMD and PyMoL packages.

Time-resolved fluorescence analysis

Time-resolved fluorescence decays ($F(t)$) were described using a multi-exponential model (Equation 13):

$$F_{norm}(t) = \sum_{i}^{n} x_i\left(t \Big/ \tau_{DA}^{(i)}\right) \quad \text{(Equation 13)}$$

where χ_i is the i-th population fraction, and $\tau_{DA}^{(i)}$ is the fluorescence lifetime of that population. Fluorescence decays from heterodimers were analyzed using a single or double exponential model, obtaining the respective χ^2_r to compare both models and to choose, using the F-test criteria, the statistically more robust behavior.

Burst variance analysis

To compute the burst variance,[49,66] single-molecule events also called "bursts" were divided into segments of equal numbers of photon (m) segments. For each segment, the corrected FRET efficiency and its variance within the burst (s^2) is calculated. To observe the contribution of dynamics beyond the shot noise, we use the shot noise variance as

$$\sigma^2 = \frac{\langle E\rangle(1 - \langle E\rangle)}{m} \quad \text{(Equation 14)}$$

where E is the corrected FRET efficiency and m is the number of photons for each segment. Hence, the excess variance (S^2) due to dynamics is

$$S^2 = s^2 - \sigma^2 \quad \text{(Equation 15)}$$

The mean excess variance (S^2) as a function of the mean duration of m-photon segments was fit to a single exponential decay to determine an effective equilibrium time. The script used is available at github.com/SMB-Lab/feda_tools.

Photon distribution analysis

We used probability distribution analysis (PDA)[46,47] to model the anisotropy and FRET efficiency distributions to identify mean anisotropy values and FRET distances between disordered ensembles and folded states ($\langle R_{DA} \rangle_E$) and their corresponding uncertainties. To properly account for the heterogeneity in the duration of bursts, bursts are split into equal time windows per burst with multiple time window sizes (Δt = 1, 3, and 10 ms), and the respective indicator histogram is obtained for each time window size. We globally fit all time windows with different models that vary in increasing level of complexity, and the best model is selected based on the global figure of merit χ_r^2. A static model considering one and two states was insufficient to fully describe the histograms at these time windows.

Filtered FCS

fFCS was accomplished by selecting the single-molecule burst to differentiate the fluorescence photons of the DA-labeled samples from background photons. Then the fluorescence species was auto-correlated based on the detection spectral window (Green, G, and Red, R) to generate four correlation curves ($G_{GG}^{(DA)}(t_c), G_{RR}^{(DA)}(t_c), G_{GR}^{(DA)}(t_c), G_{RG}^{(DA)}(t_c)$), where the subscripts correspond to the spectral window. The superscript in parentheses is the labeled species that is observed. These correspond to the color auto- and cross-correlation function of the FRET-labeled samples at single-molecule resolution. Details on the procedure can be found elsewhere.[50,51]

To analyze the hydrodynamic properties of monomers and dimers free or in the presence of DNA, each $G_{GG}^{(DA)}(t_c)$ was fitted with the model function (Equation 16) that considers a 3-dimensional Gaussian confocal volume to identify the characteristic time of diffusion t_D.

$$G(t_c) = \frac{1}{N}\left(\frac{1}{1+\frac{t}{\tau_D}}\right)\sqrt{\left(\frac{1}{1+\left(\frac{\omega}{z}\right)^2\frac{t}{\tau_D z}}\right)}\left(1 - A_p + A_p \exp\left(-\frac{t}{t_p}\right)\right) + B \quad \text{(Equation 16)}$$

where N is the average number of particles in the confocal volume, ω and z are the axes for the geometrical volume, $\tau_D = \frac{\omega^2}{4D}$ is the diffusion time, where D is the diffusion constant, and A_p is the amplitude of a photophysical term such as triplet state kinetics or photobleaching.

Error analysis of parameters for cross-correlation fits was performed by evaluating the chi-squared surface corresponding to the variation of each fit parameter. The error range was determined by using the F-test to compare the chi-squared values sampled from the χ^2 distribution to the presented fit and identifying the parameter range corresponding to a confidence interval of 2σ.

The auto and cross-correlated signals were fitted to Equations 17 and 18:

$$AC_{(HF-HF,LF-LF)}(t) = B + \frac{1}{N\left(1+\frac{t}{\tau_D}\right)\sqrt{1+\frac{t}{s^2\tau_D}}}\left(1 + A_L \exp\left(-\frac{t}{\tau_L}\right) - A_L + \sum_{i=1}^{3} A_i \exp\left(-\frac{t}{\tau_i}\right) - A_i\right)\left(1 + A_P \exp\left(-\frac{t}{\tau_P}\right) - A_P\right), \quad \text{(Equation 17)}$$

$$CC_{(HF-LF,LF-HF)}(t) = B + \frac{1}{N\left(1+\frac{t}{\tau_D}\right)\sqrt{1+\frac{t}{s^2\tau_D}}}\left(1 - A_{CC}\sum_{i=1}^{3} A_i \exp\left(-\frac{t}{\tau_L}\right)\right)\left(1 - A_L \exp\left(-\frac{t}{\tau_L}\right)\right)\left(1 + A_P \exp\left(-\frac{t}{\tau_P}\right) - A_P\right), \quad \text{(Equation 18)}$$

where B is the baseline value of each curve, S is the geometrical volume, τ_i and A_i are the anticorrelation time and its amplitude, and A_{CC} corresponds to the cross-correlation amplitude term. Photophysical terms are described by τ_P and A_P, which correspond to times and their amplitude, respectively. Any slower exchange and bleaching term are contained in τ_L and its related amplitude A_L. Correlation curves were fitted using Chisurf software.[67]

SUPPLEMENTAL INFORMATION

Supplemental information can be found online at https://doi.org/10.1016/j.xcrp.2024.101854.

ACKNOWLEDGMENTS

We thank Laura Finzi for discussion and suggestions on the manuscript. This work was supported by ANID through Fondo de Desarrollo Científico y Tecnológico (FONDECYT grants 1170701 to J.B., 11200729 to E.M., and 1201684 to C.A.R.-S.) and ANID Millennium Science Initiative Program ICN17_022 to C.A.R.-S. H.S. acknowledges support from the NIH (R01MH081923, 1P20GM130451, and R15CA280699) and NSF (CAREER MCB 1749778).

AUTHOR CONTRIBUTIONS

Conceptualization, E.M., N.K., H.S., J.B., C.A.R.-S.; validation, E.M., T.P., H.S.; formal analysis and investigation, N.K., E.M., T.P., R.G., F.X.D., H.S.; writing, E.M., H.S., T.P.

DECLARATION OF INTERESTS

The authors declare no competing interests.

Received: July 14, 2023
Revised: January 5, 2024
Accepted: February 12, 2024
Published: March 12, 2024

REFERENCES

1. Fraser, P., and Bickmore, W. (2007). Nuclear organization of the genome and the potential for gene regulation. Nature *447*, 413–417. https://doi.org/10.1038/nature05916.

2. Zheng, H., and Xie, W. (2019). The role of 3D genome organization in development and cell differentiation. Nat. Rev. Mol. Cell Biol. *20*, 535–550. https://doi.org/10.1038/s41580-019-0132-4.

3. Stadhouders, R., Filion, G.J., and Graf, T. (2019). Transcription factors and 3D genome conformation in cell-fate decisions. Nature *569*, 345–354. https://doi.org/10.1038/s41586-019-1182-7.

4. Kim, J.L., Nikolov, D.B., and Burley, S.K. (1993). Co-crystal structure of TBP recognizing the minor groove of a TATA element. Nature *365*, 520–527. https://doi.org/10.1038/365520a0.

5. Heim, M.A., Jakoby, M., Werber, M., Martin, C., Weisshaar, B., and Bailey, P.C. (2003). The basic helix-loop-helix transcription factor family in plants: a genome-wide study of protein structure and functional diversity. Mol. Biol. Evol. *20*, 735–747. https://doi.org/10.1093/molbev/msg088.

6. Alber, T. (1992). Structure of the leucine zipper. Curr. Opin. Genet. Dev. *2*, 205–210. https://doi.org/10.1016/s0959-437x(05)80275-8.

7. Rodriguez-Caso, C., Medina, M.A., and Solé, R.V. (2005). Topology, tinkering and evolution of the human transcription factor network. FEBS J. *272*, 6423–6434. https://doi.org/10.1111/j.1742-4658.2005.05041.x.

8. Boija, A., Klein, I.A., Sabari, B.R., Dall'Agnese, A., Coffey, E.L., Zamudio, A.V., Li, C.H., Shrinivas, K., Manteiga, J.C., Hannett, N.M., et al. (2018). Transcription Factors Activate Genes through the Phase-Separation Capacity of Their Activation Domains. Cell *175*, 1842–1855.e16. https://doi.org/10.1016/j.cell.2018.10.042.

9. Klug, A., and Schwabe, J.W. (1995). Protein motifs 5. Zinc fingers. Faseb. J. *9*, 597–604. https://doi.org/10.1096/fasebj.9.8.7768350.

10. Tjian, R., and Maniatis, T. (1994). Transcriptional activation: a complex puzzle with few easy pieces. Cell *77*, 5–8. https://doi.org/10.1016/0092-8674(94)90227-5.

11. Reményi, A., Schöler, H.R., and Wilmanns, M. (2004). Combinatorial control of gene expression. Nat. Struct. Mol. Biol. *11*, 812–815. https://doi.org/10.1038/nsmb820.

12. Zaret, K.S., and Carroll, J.S. (2011). Pioneer transcription factors: establishing competence for gene expression. Genes Dev. *25*, 2227–2241. https://doi.org/10.1101/gad.176826.111.

13. Li, J., Dai, S., Chen, X., Liang, X., Qu, L., Jiang, L., Guo, M., Zhou, Z., Wei, H., Zhang, H., et al. (2021). Mechanism of forkhead transcription factors binding to a novel palindromic DNA site. Nucleic Acids Res. *49*, 3573–3583. https://doi.org/10.1093/nar/gkab086.

14. Alberts, B., Johnson, A., Lewis, J., Raff, M., Roberts, K., and Walter, P. (2002). Molecular Biology of the Cell, 4th edition Edition (Garland Science).

15. Reiter, F., Wienerroither, S., and Stark, A. (2017). Combinatorial function of transcription factors and cofactors. Curr. Opin. Genet. Dev. *43*, 73–81. https://doi.org/10.1016/j.gde.2016.12.007.

16. Takahashi, H., Takahashi, K., and Liu, F.-C. (2009). FoxP Genes, Neural Development, Speech and Language Disorders. In Forkhead Transcription Factors: Vital Elements in Biology and Medicine (Springer Science+Buisness Media)), pp. 117–129.

17. Medina, E., Villalobos, P., Hamilton, G.L., Komives, E.A., Sanabria, H., Ramírez-Sarmiento, C.A., and Babul, J. (2020). Intrinsically Disordered Regions of the DNA-Binding Domain of Human FoxP1 Facilitate Domain Swapping. J. Mol. Biol. *432*, 5411–5429. https://doi.org/10.1016/j.jmb.2020.07.017.

18. Chen, Y., Chen, C., Zhang, Z., Liu, C.C., Johnson, M.E., Espinoza, C.A., Edsall, L.E., Ren, B., Zhou, X.J., Grant, S.F.A., et al. (2015). DNA binding by FOXP3 domain-swapped dimer suggests mechanisms of long-range chromosomal interactions. Nucleic Acids Res. *43*, 1268–1282. https://doi.org/10.1093/nar/gku1373.

19. Coñuecar, R., Asela, I., Rivera, M., Galaz-Davison, P., González-Higueras, J., Hamilton, G.L., Engelberger, F., Ramírez-Sarmiento, C.A., Babul, J., Sanabria, H., and Medina, E. (2023). DNA facilitates heterodimerization between human transcription factors FoxP1 and FoxP2 by increasing their conformational flexibility. iScience *26*, 107228. https://doi.org/10.1016/j.isci.2023.107228.

20. Stroud, J.C., Wu, Y., Bates, D.L., Han, A., Nowick, K., Paabo, S., Tong, H., and Chen, L. (2006). Structure of the forkhead domain of FOXP2 bound to DNA. Structure *14*, 159–166. https://doi.org/10.1016/j.str.2005.10.005.

21. Chu, Y.P., Chang, C.H., Shiu, J.H., Chang, Y.T., Chen, C.Y., and Chuang, W.J. (2011). Solution structure and backbone dynamics of the DNA-binding domain of FOXP1: insight into its domain swapping and DNA binding. Protein Sci. *20*, 908–924. https://doi.org/10.1002/pro.626.

22. Perumal, K., Dirr, H.W., and Fanucchi, S. (2015). A Single Amino Acid in the Hinge Loop Region of the FOXP Forkhead Domain is Significant for Dimerisation. Protein J. *34*, 111–121. https://doi.org/10.1007/s10930-015-9603-4.

23. Morris, G., and Fanucchi, S. (2016). A Key Evolutionary Mutation Enhances DNA Binding of the FOXP2 Forkhead Domain. Biochemistry *55*, 1959–1967. https://doi.org/10.1021/acs.biochem.5b01271.

24. Medina, E., Córdova, C., Villalobos, P., Reyes, J., Komives, E.A., Ramírez-Sarmiento, C.A., and Babul, J. (2016). Three-Dimensional Domain Swapping Changes the Folding Mechanism of the Forkhead Domain of FoxP1. Biophys. J. *110*, 2349–2360. https://doi.org/10.1016/j.bpj.2016.04.043.

25. Bandukwala, H.S., Wu, Y., Feuerer, M., Chen, Y., Barboza, B., Ghosh, S., Stroud, J.C., Benoist, C., Mathis, D., Rao, A., and Chen, L. (2011). Structure of a domain-swapped FOXP3 dimer on DNA and its function in regulatory T cells. Immunity *34*, 479–491. https://doi.org/10.1016/j.immuni.2011.02.017.

26. Leng, F., Zhang, W., Ramirez, R.N., Leon, J., Zhong, Y., Hou, L., Yuki, K., van der Veeken, J., Rudensky, A.Y., Benoist, C., and Hur, S. (2022). The transcription factor FoxP3 can fold into two dimerization states with divergent implications for regulatory T cell function and immune homeostasis. Immunity *55*, 1354–1369.e8. https://doi.org/10.1016/j.immuni.2022.07.002.

27. Sollis, E., Graham, S.A., Vino, A., Froehlich, H., Vreeburg, M., Dimitropoulou, D., Gilissen, C., Pfundt, R., Rappold, G.A., Brunner, H.G., et al. (2016). Identification and functional characterization of variants provides novel insights into the etiology of neurodevelopmental disorder. Hum. Mol. Genet. *25*, 546–557. https://doi.org/10.1093/hmg/ddv495.

28. Han, L., Chen, M., Wang, Y., Wu, H., Quan, Y., Bai, T., Li, K., Duan, G., Gao, Y., Hu, Z., et al. (2019). Pathogenic missense mutation pattern of forkhead box genes in neurodevelopmental disorders. Mol. Genet. Genomic Med. *7*, e00789. https://doi.org/10.1002/mgg3.789.

29. Keeler, J.D., and Sharma, R.P. (1975). Rabbit erythrocyte membrane interaction with promazine and calcium. Biochem. Pharmacol. *24*, 2207–2211. https://doi.org/10.1016/0006-2952(75)90053-2.

30. Hellenkamp, B., Schmid, S., Doroshenko, O., Opanasyuk, O., Kühnemuth, R., Rezaei Adariani, S., Ambrose, B., Aznauryan, M., Barth, A., Birkedal, V., et al. (2018). Precision and accuracy of single-molecule FRET measurements-a multi-laboratory benchmark study. Nat. Methods *15*, 669–676. https://doi.org/10.1038/s41592-018-0085-0.

31. Agam, G., Gebhardt, C., Popara, M., Mächtel, R., Folz, J., Ambrose, B., Chamachi, N., Chung, S.Y., Craggs, T.D., de Boer, M., et al. (2023). Reliability and accuracy of single-molecule FRET studies for characterization of structural dynamics and distances in proteins. Nat. Methods *20*, 523–535. https://doi.org/10.1038/s41592-023-01807-0.

32. Fries, J.R., Brand, L., Eggeling, C., Köllner, M., and Seidel, C.A.M. (1998). Quantitative identification of different single molecules by selective time-resolved confocal fluorescence spectroscopy. J. Phys. Chem. A *102*, 6601–6613. https://doi.org/10.1021/jp980965t.

33. Widengren, J., Kudryavtsev, V., Antonik, M., Berger, S., Gerken, M., and Seidel, C.A.M. (2006). Single-molecule detection and identification of multiple species by multiparameter fluorescence detection. Anal. Chem. *78*, 2039–2050. https://doi.org/10.1021/ac0522759.

34. Barth, A., Opanasyuk, O., Peulen, T.O., Felekyan, S., Kalinin, S., Sanabria, H., and Seidel, C.A.M. (2022). Unraveling multi-state molecular dynamics in single-molecule FRET experiments. I. Theory of FRET-lines. J. Chem. Phys. *156*, 141501. https://doi.org/10.1063/5.0089134.

35. Opanasyuk, O., Barth, A., Peulen, T.O., Felekyan, S., Kalinin, S., Sanabria, H., and Seidel, C.A.M. (2022). Unraveling multi-state molecular dynamics in single-molecule FRET experiments. II. Quantitative analysis of multi-state kinetic networks. J. Chem. Phys. *157*, 031501. https://doi.org/10.1063/5.0095754.

36. Sanabria, H., Rodnin, D., Hemmen, K., Peulen, T.O., Felekyan, S., Fleissner, M.R., Dimura, M., Koberling, F., Kühnemuth, R., Hubbell, W., et al. (2020). Resolving dynamics and function of transient states in single enzyme molecules. Nat. Commun. *11*, 1231. https://doi.org/10.1038/s41467-020-14886-w.

37. Tsytlonok, M., Sanabria, H., Wang, Y., Felekyan, S., Hemmen, K., Phillips, A.H., Yun, M.K., Waddell, M.B., Park, C.G., Vaithiyalingam, S., et al. (2019). Dynamic anticipation by Cdk2/Cyclin A-bound p27 mediates signal integration in cell cycle regulation. Nat. Commun. *10*, 1676. https://doi.org/10.1038/s41467-019-09446-w.

38. Yanez Orozco, I.S., Mindlin, F.A., Ma, J., Wang, B., Levesque, B., Spencer, M., Rezaei Adariani, S., Hamilton, G., Ding, F., Bowen, M.E., and Sanabria, H. (2018). Identifying weak interdomain interactions that stabilize the supertertiary structure of the N-terminal tandem PDZ domains of PSD-95. Nat. Commun. *9*, 3724. https://doi.org/10.1038/s41467-018-06133-0.

39. Saikia, N., Yanez-Orozco, I.S., Qiu, R., Hao, P., Milikisiyants, S., Ou, E., Hamilton, G.L., Weninger, K.R., Smirnova, T.I., Sanabria, H., and Ding, F. (2021). Integrative structural dynamics probing of the conformational heterogeneity in synaptosomal-associated protein 25. Cell Rep. Phys. Sci. *2*, 100616. https://doi.org/10.1016/j.xcrp.2021.100616.

40. Hamilton, G.L., Saikia, N., Basak, S., Welcome, F.S., Wu, F., Kubiak, J., Zhang, C., Hao, Y., Seidel, C.A.M., Ding, F., et al. (2022). Fuzzy supertertiary interactions within PSD-95 enable ligand binding. Elife *11*, e77242. https://doi.org/10.7554/eLife.77242.

41. Tsytlonok, M., Hemmen, K., Hamilton, G., Kolimi, N., Felekyan, S., Seidel, C.A.M., Tompa, P., and Sanabria, H. (2020). Specific Conformational Dynamics and Expansion Underpin a Multi-Step Mechanism for Specific Binding of p27 with Cdk2/Cyclin A. J. Mol. Biol. *432*, 2998–3017. https://doi.org/10.1016/j.jmb.2020.02.010.

42. Hofmann, H., Soranno, A., Borgia, A., Gast, K., Nettels, D., and Schuler, B. (2012). Polymer scaling laws of unfolded and intrinsically disordered proteins quantified with single-molecule spectroscopy. Proc. Natl. Acad. Sci. USA *109*, 16155–16160. https://doi.org/10.1073/pnas.1207719109.

43. Tesei, G., Trolle, A.I., Jonsson, N., Betz, J., Pesce, F., Johansson, K.E., and Lindorff-Larsen, K. (2023). Conformational ensembles of the human intrinsically disordered proteome: Bridging chain compaction with function and sequence conservation. Preprint at bioRxiv. 2023-2005. https://doi.org/10.1101/2023.05.08.539815.

44. Tesei, G., and Lindorff-Larsen, K. (2022). Improved predictions of phase behaviour of intrinsically disordered proteins by tuning the interaction range. Open Res. Eur. *2*, 94. https://doi.org/10.12688/openreseurope.14967.2.

45. Möckel, C., Kubiak, J., Schillinger, O., Kühnemuth, R., Della Corte, D., Schröder, G.F., Willbold, D., Strodel, B., Seidel, C.A.M., and Neudecker, P. (2019). Integrated NMR, Fluorescence, and Molecular Dynamics Benchmark Study of Protein Mechanics and Hydrodynamics. J. Phys. Chem. B *123*, 1453–1480. https://doi.org/10.1021/acs.jpcb.8b08903.

46. Kalinin, S., Felekyan, S., Antonik, M., and Seidel, C.A.M. (2007). Probability distribution analysis of single-molecule fluorescence anisotropy and resonance energy transfer. J. Phys. Chem. B *111*, 10253–10262. https://doi.org/10.1021/jp072293p.

47. Kalinin, S., Sisamakis, E., Magennis, S.W., Felekyan, S., and Seidel, C.A.M. (2010). On the origin of broadening of single-molecule FRET efficiency distributions beyond shot noise limits. J. Phys. Chem. B *114*, 6197–6206. https://doi.org/10.1021/jp100025v.

48. Kalinin, S., Valeri, A., Antonik, M., Felekyan, S., and Seidel, C.A.M. (2010). Detection of structural dynamics by FRET: a photon distribution and fluorescence lifetime analysis of systems with multiple states. J. Phys. Chem. B *114*, 7983–7995. https://doi.org/10.1021/jp102156t.

49. Torella, J.P., Holden, S.J., Santoso, Y., Hohlbein, J., and Kapanidis, A.N. (2011). Identifying molecular dynamics in single-molecule FRET experiments with burst variance analysis. Biophys. J. *100*, 1568–1577. https://doi.org/10.1016/j.bpj.2011.01.066.

50. Felekyan, S., Kalinin, S., Sanabria, H., Valeri, A., and Seidel, C.A.M. (2012). Filtered FCS: species auto- and cross-correlation functions highlight binding and dynamics in biomolecules. ChemPhysChem *13*, 1036–1053. https://doi.org/10.1002/cphc.201100897.

51. Felekyan, S., Sanabria, H., Kalinin, S., Kühnemuth, R., and Seidel, C.A.M. (2013). Analyzing Forster resonance energy transfer with fluctuation algorithms. Methods Enzymol. *519*, 39–85. https://doi.org/10.1016/B978-0-12-405539-1.00002-6.

52. Medina, E., R Latham, D., and Sanabria, H. (2021). Unraveling protein's structural dynamics: from configurational dynamics to ensemble switching guides functional mesoscale assemblies. Curr. Opin. Struct. Biol. *66*, 129–138. https://doi.org/10.1016/j.sbi.2020.10.016.

53. Kim, J.H., Hwang, J., Jung, J.H., Lee, H.J., Lee, D.Y., and Kim, S.H. (2019). Molecular networks of FOXP family: dual biologic functions, interplay with other molecules and clinical implications in cancer progression. Mol. Cancer *18*, 180. https://doi.org/10.1186/s12943-019-1110-3.

54. Wu, Y., Borde, M., Heissmeyer, V., Feuerer, M., Lapan, A.D., Stroud, J.C., Bates, D.L., Guo, L., Han, A., Ziegler, S.F., et al. (2006). FOXP3 controls regulatory T cell function through cooperation with NFAT. Cell *126*, 375–387. https://doi.org/10.1016/j.cell.2006.05.042.

55. Bustamante, A., Rivera, R., Floor, M., Babul, J., and Baez, M. (2021). Single-molecule optical tweezers reveals folding steps of the domain swapping mechanism of a protein. Biophys. J. *120*, 4809–4818. https://doi.org/10.1016/j.bpj.2021.09.026.

56. Häußermann, K., Young, G., Kukura, P., and Dietz, H. (2019). Dissecting FOXP2 Oligomerization and DNA Binding. Angew. Chem., Int. Ed. Engl. *58*, 7662–7667. https://doi.org/10.1002/anie.201901734.

57. Sollis, E., Graham, S.A., Vino, A., Froehlich, H., Vreeburg, M., Dimitropoulou, D., Gilissen, C., Pfundt, R., Rappold, G.A., Brunner, H.G., et al. (2016). Identification and functional characterization of de novo FOXP1 variants provides novel insights into the etiology of neurodevelopmental disorder. Hum. Mol. Genet. *25*, 546–557. https://doi.org/10.1093/hmg/ddv495.

58. Zhang, F., Meng, G., and Strober, W. (2008). Interactions among the transcription factors Runx1, RORgammat and Foxp3 regulate the differentiation of interleukin 17-producing T cells. Nat. Immunol. *9*, 1297–1306. https://doi.org/10.1038/ni.1663.

59. Deng, G., Song, X., Fujimoto, S., Piccirillo, C.A., Nagai, Y., and Greene, M.I. (2019). Foxp3 Post-translational Modifications and Treg Suppressive Activity. Front. Immunol. *10*, 2486. https://doi.org/10.3389/fimmu.2019.02486.

60. Sołtys, K., and Ożyhar, A. (2021). Transcription Regulators and Membraneless Organelles Challenges to Investigate Them. Int. J. Mol. Sci. *22*, 12758. https://doi.org/10.3390/ijms222312758.

61. Gomes, E., and Shorter, J. (2019). The molecular language of membraneless organelles. J. Biol. Chem. *294*, 7115–7127. https://doi.org/10.1074/jbc.TM118.001192.

62. Wallmann, A., and Kesten, C. (2020). Common Functions of Disordered Proteins across Evolutionary Distant Organisms. Int. J. Mol. Sci. *21*, 2105. https://doi.org/10.3390/ijms21062105.

63. Ma, J., Yanez-Orozco, I.S., Rezaei Adariani, S., Dolino, D., Jayaraman, V., and Sanabria, H. (2017). High Precision FRET at Single-molecule Level for Biomolecule Structure Determination. J. Vis. Exp. 55623. https://doi.org/10.3791/55623.

64. Lakowicz, J.R. (2006). Principles of Fluorescence Spectroscopy (Springer).

65. Sindbert, S., Kalinin, S., Nguyen, H., Kienzler, A., Clima, L., Bannwarth, W., Appel, B., Müller, S., and Seidel, C.A.M. (2011). Accurate distance determination of nucleic acids via Forster resonance energy transfer: implications of dye linker length and rigidity. J. Am. Chem. Soc. *133*, 2463–2480. https://doi.org/10.1021/ja105725e.

66. Terterov, I., Nettels, D., Makarov, D.E., and Hofmann, H. (2023). Time-resolved burst variance analysis. Biophys. Rep. *3*, 100116. https://doi.org/10.1016/j.bpr.2023.100116.

67. Peulen, T.O., Opanasyuk, O., and Seidel, C.A.M. (2017). Combining Graphical and Analytical Methods with Molecular Simulations To Analyze Time-Resolved FRET Measurements of Labeled Macromolecules Accurately. J. Phys. Chem. B *121*, 8211–8241. https://doi.org/10.1021/acs.jpcb.7b03441.

68. Xue, B., Dunbrack, R.L., Williams, R.W., Dunker, A.K., and Uversky, V.N. (2010). PONDR-FIT: a meta-predictor of intrinsically disordered amino acids. Biochim. Biophys. Acta *1804*, 996–1010. https://doi.org/10.1016/j.bbapap.2010.01.011.